Additive Manufacturing 41 (2021) 101967

Contents lists available at ScienceDirect

Additive Manufacturing

journal homepage: www.elsevier.com/locate/addma

Research Paper

Rheology scaling of spherical metal powders dispersed in thermoplastics and its correlation to the extrudability of filaments for 3D printing

Amm G. Hasib [a], Stanislau Niauzorau [a], Weiheng Xu [a], Sridhar Niverty [b], Natalya Kublik [a], Jason Williams [c], Nikhilesh Chawla [b], Kenan Song [a,*], Bruno Azeredo [a,*]

[a] The Polytechnic School (TPS), Ira A. Fulton Schools of Engineering, Arizona State University, Mesa, AZ 85281, USA
[b] School of Materials Engineering, College of Engineering, Purdue University, West Lafayette, IN 47907, USA
[c] Center for 4D Materials Science, Materials Science and Engineering, Arizona State University, 501 E. Tyler Mall, ECG 303, Tempe, AZ 85287-6106, USA

ARTICLE INFO

Keywords:
Material extrusion
Metal additive manufacturing
Rheological behavior
Metal composite
Powder metals
Sintering
Highly filled polymers
Jamming
Shrinkage

ABSTRACT

3D printing metals via material extrusion utilizes a metal particle reinforced polymer matrix composite (PMC) as the filament which is typically made with gas-atomized powders as fillers. Its rheological behavior limits the maximum metal content of the printed green composite which, consequently, hinders further reductions to part porosity and shrinkage. In this paper, the scaling of the dynamic viscosity of melt-extruded PMC filaments made of PLA and Ni-Cu gas-atomized powders is studied as a function of the metal's volumetric content and feedstock pre-mixing strategies and correlated to its extrudability performance. Extrudable and uniform filaments with the highest metal content of 63.4 vol% were produced by employing solution-mixing of the PMC feedstock and compared to physical mixing which only reached 54 vol%. After sintering, the improved metal content of 3D printed parts from solution-mixing reduced linear shrinkage by 76% in comparison to physical mixing, resulting in an absolute shrinkage value of 0.49%. By characterizing the PMC feedstock via flow-sweep rheology tests, a distinct extension of the shear-thinning zone towards high shear rates (i.e. 100 s^{-1}) at high metal content was observed for the case of solution-mixed feedstock – a result that is attributed to the improved adhesion of the PMCs to the walls of the rheometer. PMCs with such characteristics correlated well to favorable extrudability and windability test outcomes (i.e. no particle jamming or metal accumulation at the die). The Krieger-Dougherty analytical model was employed to predict the zero-shear rate viscosity as a function of the metal content in the PMCs, however, the latter property is not necessarily correlated to the viscosity at high shear rates (10–1000 s^{-1}) due to a complex shear thinning response. Since PMCs experience high shear rates in the die orifice, additional theoretical models are needed to predict shear-thinning at high metal content in PMCs and, thus, improve our prediction of PMC's rheology, its design, and extrudability to maximize its metal content.

1. Introduction

Metal additive manufacturing via material extrusion (a.k.a. Fused Filament Fabrication or FFF) offers low-tooling costs, table-top systems, user-friendliness [1], reduced powder handling needs and hazards, and multi-material printing capabilities [2] in comparison with well-established approaches such as selective laser sintering (SLS) [3], selective laser melting (SLM) [4,5], directed energy deposition (DED) [6] and metal binder jetting [7,8]. As a result, it can be installed inside commercial, residential and research settings, distributing manufacturing near design teams, home users, and hobbyists to facilitate design iteration [9]. However, metal-based material extrusion has its own drawbacks, such as the need for debinding the thermoplastic, surface roughness [10], high part shrinkage that limits dimensional tolerances, and significant level of part porosity due to pores between tracks and metallic powders that limits mechanical strength [11]. The latter two limitations originate during filament extrusion [12] since they are both mitigated by increasing the metal content of the resulting green parts.

Thus, to print denser green parts, it becomes necessary to understand the role of shear-thinning in the PMCs during extrusion [13]. Recent literature explores the effects of the powder size distribution [14–18], powder shape [19,20], and the interfacial adhesions [21] between the metal and thermoplastic to minimize the viscosity of the melt.

---

* Corresponding authors.
E-mail addresses: kenan.song@asu.edu (K. Song), bruno.azeredo@asu.edu (B. Azeredo).

https://doi.org/10.1016/j.addma.2021.101967
Received 5 December 2020; Received in revised form 15 February 2021; Accepted 19 March 2021

Non-spherical metal fillers often exhibit limited flowability as they are plagued by mechanical interlocking, which is a function of particle size and shape and which often promotes clustering [22,23]. Studies revealed the advantages of gas atomized metal particles over water atomized and ball-milled powders not only from the perspective of rheology, but also from the perspective of achieving homogeneity, higher packing factor, and greater part density after sintering [14,20,24]. Additionally, maintaining the homogeneity of highly filled metals in the thermoplastic matrix is critical [23,25,26], as particles are more prone to aggregation, leading to mechanical interlocking in highly concentrated PMCs [23]. Attempts to quantify dispersion were only limited to either simulation and theoretical studies [27,28] or non-metal fillers and nanocomposites [29–32], often undergoing solid-state mixing (i.e. ball mill and traditional mixing) [23,33,34].

As the metal content reaches more than 55 vol%, homogeneity of metal dispersion in the PMC feedstock prior to extrusion plays a vital role in preventing the particle jamming in the extruder. The so-called “traditional mixing” method relies on the physical mixing of dry polymer and metal powders typically in a low energy stirring mixer to homogenize the feedstock prior to extrusion, where additional mixing takes place in the melt inside the extruder’s barrel due to the action of the reciprocating screw [35]. However, mixing inside the barrel by the action of the screw does not always provide enough circulation for enabling sufficient mixing, particularly in the case of thermoplastics with high melt viscosity that promotes laminar flow [36]. Moreover, winding the extrudate in a spool of PMC filaments with a metal content of more than 40 vol% becomes difficult due to its high stiffness and brittleness [37] for it to be bent into the desired radius of curvature.

In this paper, a compatible solvent-based solution pre-mixing strategy [38] was adopted and metal particle distribution and homogeneity in PMC were compared with the traditional approach for fabricating filaments using a popular single-barrel extruder from Noztek. The extrudability and windability of PMC filaments composed of PLA and gas atomized Ni-Cu powder were tested from low (28 vol%) to high (63.4 vol%) metal loading in gradual increments as a function of the physical and solution pre-mixing strategies. It was revealed that the solution-mixed feedstock attained a maximum metal loading of 62 vol% that passed both the extrudability and windability criteria of extrusion tests and a maximum metal loading of 63.4 vol% that passed the extrudability test only. In contrast, the physically-mixed feedstock only reached the highest extrudable filament content of 54 vol% metal and the highest windable filament content of 43 vol% metal. Additionally, the homogeneity of the metal in the filaments as a function of its content is characterized in detail via thermogravimetric analysis (TGA).

While examining the rheology of the melted composite via flow sweep rheology test and dynamic mechanical testing (DMA), it was sought to understand (i) predictors of the extrudability of the PMCs as well as (ii) the scaling of the viscosity at both low and high shear rates. In a flow sweep rheology test, the zero-shear viscosity of PMCs was measured and found to scale as a function of metal content for both the physically- and the solution-mixed precursors in close agreement with the theoretical model by Krieger and Dougherty [39] for monodispersed rigid spheres. Also, the flow sweep tests suggest that physically-mixed feedstock is more prone to slippage at the high-shear rate ranges imposed by the die (i.e. between 10 and 1000 s^{-1}). SAOS (Small amplitude oscillatory shear) test was conducted to demonstrate the materials behavior shift from viscoelastic state to elastic solid state as a function of metal content [40].

Next, the dimensional shrinkage of 3D printed parts measured after sintering was found to be inversely proportional to the initial volumetric metal content of the green part. In summary, this work not only represents a framework for studying highly packed and homogenously dispersed metal particles for PMC filament production but also sheds light on the complexity of the rheological scaling of PMCs with increasing filler content, which becomes increasingly relevant (i) to increase the green part density and (ii) to improve extrudability of unconventional PMC fillers such as space-mined and cementitious materials, and nanomaterials for novel 3D printing applications.

2. Materials and method

2.1. Materials

Semi-crystalline and biodegradable [41] polymer PLA pellets (pulverized and procured from Filabot with a vendor-reported M_w ~170, 000 g/mol, density 1.25 g/cm^3 and average pellet size of 2.5 mm; see Fig. S1 from the supplementary section) was chosen to perform all the extrusion and rheology tests conducted in this study. Gas atomized Ni–Cu powders (68 wt% Cu and 32 wt% Ni with a vendor-reported density of 8.94 g/cm^3) with a median particle size of 62.4 μm (see Fig. S2 and Table S1 from the supplementary section) were procured from PAC (Powder Alloy Corporation) to be used as our metal fillers.

2.2. Manufacturing method

2.2.1. Mixing

Two methods were selected for mixing of the polymer and metal prior to extrusion and termed as “physical mixing” and “solution mixing”. For the physical mixing method, vacuum dried pulverized PLA was blended in a solid phase with Ni-Cu powders and transferred to a plastic bag. For the solution mixing method, vacuum dried PLA was added into a beaker with DCM (dichloromethane) with a 1:10 (w/v) ratio (which suggests for every 1 g of PLA to dissolve, 10 ml DCM was used) and magnetically stirred (350 rpm) on a hotplate at 35 °C for 4–6 h to allow complete dissolution. Subsequently, pre-weighed NiCu alloy powders were added gradually with the aid of the elevated hotplate temperature (60 °C) and mechanically stirred for an hour to get a thick paste-like suspension as the solvent evaporated. The suspension was poured into a handmade aluminum foil boat and dried in a vacuum furnace at 60 °C for 4 h and after that, it was kept for natural drying for 24 h in a fume hood. After drying, the thick paste turned into a solid chunk and cut into an average of 5 mm pieces by a steel strapping cutter to get the final feedstock feedable into the extruder’s hopper (see Fig. S5 from the supplementary section). The details of the solution mixing process along with extrusion, winding and 3D printing are shown in Fig. 1.

2.2.2. Extrusion

Extrusion was performed at 180 °C (heaters placed before the die and at the end of the compression zone were maintained at the same temperature) in a desktop single screw extruder (model name: “Noztek Touch ” manufactured by Noztek) with a standard dual PID and variable motor speed control. The extruder motor speed was varied between 30 and 40 rpm (30 rpm for $<$ 50 vol% metal loading and 40 rpm for $>$50 vol% metal loading). Increasing the rotational speed was necessary to synchronize the extrusion output rate with the winding speed at higher metal loading. The extrusion-die I.D was 2.85 mm. After extrusion, all the filaments passed above a small extruder fan to lower down the filament temperature, and then filaments were winded in a 100 mm diameter spool which was kept at a one-foot distance from the die. All filament extrusions were carried out following a standard protocol which includes (i) turning on the heating elements of the extruder and waiting for at least 15 min after the controller reaches extrusion temperature (180 °C) to ensure heat equilibration inside the barrel, (ii) turning on the motor and manually loading the PMC feedstock while adjusting its loading rate to maintain the hopper fill level constant at about one half of its maximum capacity and keeping the motor speed constant, (iii) allowing the PMC feedstock to be extruded for 5–10 min to stabilize the flow before collecting 12-ft filaments for further characterization, (iv) at the end of PMC’s extrusion, cleaning the barrel by flushing dried PLA for 5–10 min after a single run to purge any materials accumulated inside the barrel, and (v) not running more than two weeks without deep cleaning it (i.e. open apart the barrel and the screw, and

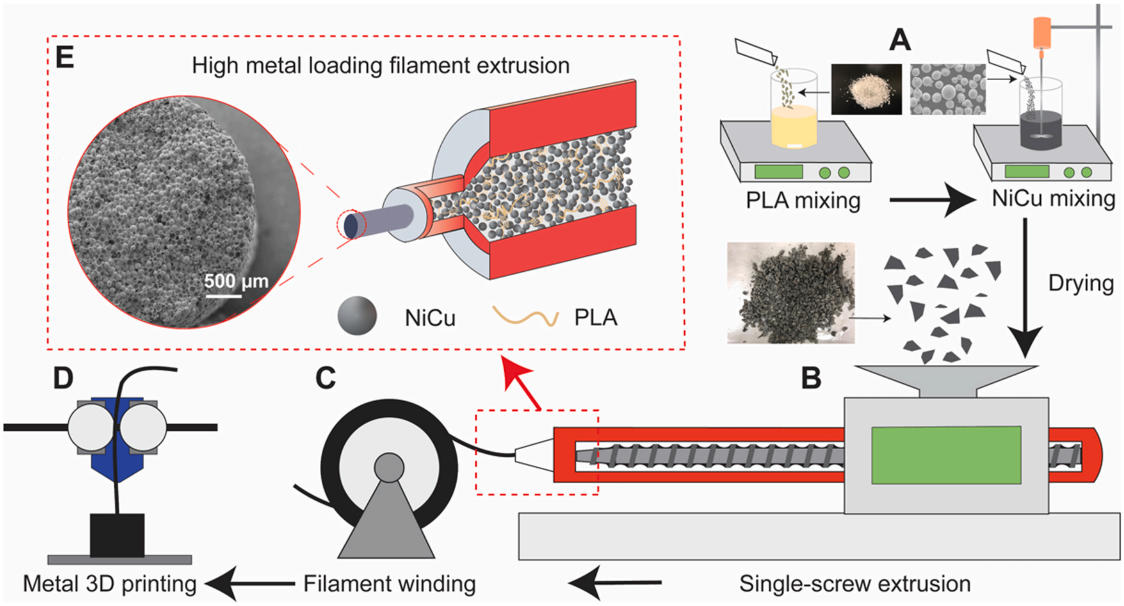

Fig. 1. Process overview: (A) solution mixing of PLA with DCM and Ni–Cu, (B) single screw extrusion, (C) winding of PMC filament in a spool, (D) 3D printing with the PMC filament, and (E) high metal loading filament extrusion (62 vol% metal filament in the magnified SEM image).

clean the inside thoroughly with a metal brush and a heat gun).

2.2.3. *Extrusion and winding experiment design*

Experiments were designed to quantify the homogeneity of metal particle dispersion and to study the PMC filament's melt rheology with increasing metal content. A strict predefined protocol (mentioned in the extrusion section) was maintained and an experimental framework for extrudability and windability was created which is described in Tables 1 and 2. Five different sets of feedstocks were prepared for extrusion for each mixing method starting from the pre-mix content of 70 wt% (25 vol %) metal and then increasingly to 80%, 85%, 87.5% and 90 wt% (36%, 44%, 50%, and 56 vol% consecutively). At 56 vol% content of metal, physically-mixed feedstocks failed both the extrudability and windability criteria in the extrusion test. Hence, additional feedstocks of 92, 92.5, and 92.55 wt% (i.e. 62%, 63.4%, and 63.5 vol% respectively) of metals were prepared via solution mixing only. For all specimens, 12 ft of stable and continuously extruded filaments were collected for further analysis. Also, the windability criterion was based on a set-up with very short distances (i.e. 1 ft) between the extruder's die and the winder, and, as a result, the filament was still hot during winding and it formed with the curvature of the spool (i.e. it is not straight). Note that this did not follow industry standards.

Table 1
Terminology of different terms used in the experimental framework.

Terms Used	Definition
Extrudability (Pass/Fail)	The ability to continuously collect at least 12 ft long uniform filament fabricated by material extrusion was termed as **"Pass"**, and, otherwise, termed as "**Fail**" if filaments broke before 12 ft due to "melt fracture" or "nozzle clogging".
Windability (Pass/Fail)	The ability to wind at least 12 ft long uniform filaments in a 100 mm diameter spool without any breakage due to brittleness/stiffness was termed as "**Pass**", and otherwise, termed as **"Fail"** if filaments broke due to brittleness. This criterion may be changed according to the change of spool diameter and temperature of the filament during winding
Global dispersion homogeneity or uniformity	Homogeneity of metal particle dispersions in the entire 12 ft long filament measured by TGA. Pieces were cut from the filament at every two feet sections to measure the metal concentration variation via TGA. Each piece removed from a different filament section was about 15–20 mg by weight.
Local dispersion homogeneity or uniformity	Homogeneity of metal particle distribution in a random filament section measured by micro-X-ray tomography. Filament volume probed was 2–3 cm in length with an average diameter of 2.75 mm

2.2.4. *3D Printing*

Multiple 1 cm^3 cubes of varying metal content were 3D printed with a layer thickness set to 0.2 mm, infill density 100%, and print speed of 20 mm/s using a desktop 3D printer Ultimaker 3. The glass printing bed was preheated to 60 °C for better thermal distribution and a matte blue gaffer tape was used on top of the print bed to promote better adhesion with the base layer. The detailed 3D printing parameters are listed in Table S4 of the supplementary section.

2.2.5. *Sintering*

The green 3D printed cubes were placed inside a smelting graphite crucible surrounded by sintering refractory ballast composed of alumina and graphite powders. The refractory ballast materials acted as a solid mold to conform to the shape of the printed part. The samples were loaded into a tube furnace with ultra-high pure (99.999%) Argon atmosphere and debinded with a very slow ramp rate (0.2 °C/min) up to 420 °C (slightly more than the polymer degradation temperature) to ensure the dimensional integrity is not destroyed while PLA was boiled and sublimed away from the printed structure. A 5 °C/min ramp rate was used from 420 °C to reach the sintering temperature of 1061 °C (around 93% of the Ni–Cu alloy melting temperature [42]) to hold there for 5 h allowing necking growth and densification.

2.3. *Thermal characterization by TGA and DSC*

All the filament samples collected for the extrusion test were 12 ft in length and passed the desired extrudability test according to a predefined protocol (**protocol described in the extrusion section**) except for 56 vol% physically-mixed filament sample, which broke a couple of times during the extrusion before reaching 12 ft. However, uniform filaments of 56 vol% physically-mixed filament were collected as a rod to test its homogeneity of dispersion and suspension rheology. From every 2 ft out of 12 ft filament, a small cross-section (weighing less than 20 mg) was sectioned and extracted to undergo thermogravimetric

Table 2
Extrudability and windability outcomes from two feedstock mixing process.

Pre-mix content % (before extrusion)		**Post-mix content % (after extrusion)**		**Mixing method**	**Extrudability**	**Windability**
By volume	By weight	By volume	By weight			
~63.5	~92.55	–	–	Solution mixing	Fail	Fail
63.3	92.5	63.4	92.5	Solution mixing	Pass	Fail
62.0	**92.0**	**61.9**	**92.0**	**Solution mixing**	**Pass**	**Pass**
56.0	90.0	60.9	91.5	Solution mixing	Pass	Pass
		56.5	90.3	Physical mixing	Fail	Fail
50.0	87.5	52.5	88.5	Solution mixing	Pass	Pass
		54.0	89.0	Physical mixing	Pass	Fail
44.0	85.0	49.5	87.5	Solution mixing	Pass	Pass
		47.0	86.0	Physical mixing	Pass	**Fail**
36.0	**80.0**	37.9	81.3	Solution mixing	Pass	Pass
		43.0	**84.5**	**Physical mixing**	**Pass**	**Pass**
25.0	70.0	27.8	73	Solution mixing	Pass	Pass
		28.0	73.5	Physical mixing	Pass	Pass

Source: Experimental outcome from our predefined extrudability-windability framework (motor speed= 30–40 rpm, extrusion temperature of 180 °C).

analysis (TGA) in order to determine the metal concentration inside the polymer matrix. TGA 550 (manufactured by the TA instrument) was used with a scan rate of 10 °C/min in a nitrogen-controlled atmosphere ramping the temperature from 25 °C to 500 °C. A total of five data points (five TGA measurements of metal wt% after the complete degradation of polymer around 400 °C) were taken for every 12 ft long filament sample involving all combinations of metal loading and mixing strategies, to investigate how the metal vol% varies along the filament length and that is how the global homogeneity of metal dispersion (see Table 1 and Fig. 3A) was measured. The details on the extrudability and windability criteria and homogeneity are given in Tables 1, 2, and Fig. 3. Each PMC filament metal wt% was converted to vol% by utilizing the NiCu alloy powder composition (62% Cu, 38% Ni), the density of alloy (8.94 g/cc, source: vendor PAC technical datasheet), and density of polymer (1.25 g/cc, source: vendor Filabot technical datasheet). The conversion from as designed pre-mix wt% to vol% is shown in Table S2 from the supplementary section.

To see how different PLA processing influences its microstructure, differential scanning calorimetry (DSC) (DSC 250, manufactured by TA instrument) was utilized. Less than 10 mg of dried PLA specimen were collected from different processing stages: (i) as purchased pure PLA pellets, (ii) PLA after dissolving in DCM, (iii) extrudate of pure PLA, (iv) extrudate of DCM dissolved PLA and placed inside the DSC chamber with a scan rate of 10 °C/min in a nitrogen atmosphere to see the glass transition temperature, cold crystallization temperature, and the melting point of PLA (see Fig. 5D). Note that all samples were vacuum dried before putting inside the DSC chamber. The heat-cool-reheat cycle was used to remove any thermal and processing history before the test.

2.4. Rheological characterization by flow sweep test and DMA

All rheological tests were performed on extruded filaments that were re-melted and placed in a rotational rheometer (DHR 2 manufactured by TA instrument) with a 25 mm parallel plate configuration and 400 μm gap size. To avoid the bubble effect each filament was vacuum melted in a furnace at 180 °C before transferring to the heated rheometer plate. The filament was pre-soaked for 10 min and a shear rate range of $2.8 \times 10^{-3}\ \mathrm{s}^{-1}$ to $200\ \mathrm{s}^{-1}$ was used to conduct the flow sweep rheology test at a constant (180 °C) temperature to observe the change of dynamic viscosity with increasing shear rate. This shear rate range was carefully chosen after running several tests varying the metal loading to avoid earlier slippage due to a large velocity gradient developed between the parallel plates at higher shear rates. Normally, viscosity and shear stress lines move along in the opposite direction while subjected to an increasing shear rate. Slippage is identified when an abrupt change in both the magnitude and direction of stress is observed, resulting in a drastically low viscosity and shear stress. For further analysis, high shear rate data plagued by slippage were cropped out and excluded according to the criterion described in the supplementary section (see an example of data cropping when the data is afflicted by slippage in Fig. S3). Only extrudable filaments were considered for the characterization, and the only exception to this case was *56 vol% pre-mix physically-mixed filament (i.e. 58 vol% post-mix), which was not extrudable according to our definition of 12 ft continuous extrusion, but the filament was collected for the rheology test from the stable and uniform portion of the filament rod.* For the dynamic mechanical analysis (DMA) test, a small amplitude oscillatory shear (SAOS) test was utilized to predict the viscoelastic response of the solution-mixed filaments. To ensure the most reliable data, a linear viscoelastic range was pre-determined by running a series of amplitude tests. A strain value of 0.5% with an angular frequency range of 0.1 rad/s to 500 rad/s was used for the SAOS test.

2.5. Microscopic characterization by SEM and X-ray microtomography

The filament cross-sections were prepared for SEM by dipping the filament in liquid nitrogen for 5 min to make the PLA brittle and cleaved manually to obtain a flat cross-section. Each sample (e.g. 2 cm length and 2.85 mm avg. diameter) was gold-coated with a thickness of 10–12 nm to increase its conductivity before putting into the SEM chamber. All cross-sectional images of the filaments were taken in the Phillips XL30 Environmental FEG-FEI scanning electron microscope (SEM). In addition, four filament samples were prepared (with a 2–3 cm length and 2.75 mm avg. diameter) with low (25 vol% pre-mix) and high (50 vol% pre-mix) metal content of two different mixing strategies for micro-computed X-ray tomography (micro-XCT) to see the local spatial distribution of metal particles (defined in Table 1) and to quantify the degree of metal clustering. XCT scans were performed on the extruded filament sections using a lab-scale Zeiss Versa 520 x-ray microscope (Carl Zeiss Microscopy, Pleasanton, CA, USA). All specimens were scanned with the same XCT data acquisition parameters for comparison. An accelerating voltage of 120 kV was used. 3201 projections were captured with an exposure time of 1 s per projection. A voxel size of 3.02 μm was achieved using a 4X objective lens, a camera binning of 2, and a geometric magnification (i.e. ratio of source to detector distance to the source to specimen distance) of 2.25.

3. Results and discussions

3.1. Extrudability-Windability

The inclusion of highly concentrated metal particles in polymer matrices is challenging to be extruded and winded. Improving the mixing and homogenization of the precursor feedstock is a way to facilitate the flowability of the polymer/metal composite melt inside the barrel [35]. Here, an extrusion test (defined in Table 1) was employed for comparing two precursor mixing methods: (i) physical mixing that mechanically blends solid polymer with metal powders and (ii) solution mixing in which metals are added to solvent dissolved polymer solutions, dried, and trimmed as pellets. Fig. 2 shows the morphology of filament cross-sections for both mixing methods. Fig. 2A1-B1 are SEM images of cross-sections of PMC filaments with 44 vol% and 56 vol% of post-mix metal content for physical mixing. In physically-mixed feedstocks, PMC filaments containing 44 vol% of metal were extrudable (Fig. 2A2) but not windable, while metal concentrations equal to and higher than 56 vol% led to unstable filament extrusion [12] (Fig. 2B2). In contrast, Fig. 2C showed the results for solution-mixed filaments containing 62 vol% metals, which showed uniform metal particle distributions (Fig. 2C1) and did not pose any difficulty to continuous extrusion and winding (Fig. 2C2). The maximum pre-mix metal concentration to pass both the extrusion and windability criteria was 36 vol % and 62 vol% for physical mixing and solution mixing, respectively (see Tables 1 and 2), though the post-mix actual metal concentration that passed the extrusion test was 43 vol% (see Table 2 and Fig. 3A). It was possible to successfully extrude up to 63.4 vol% metal using the solution mixing method, but it failed to meet the windability criterion. Attempt to extrude 63.5 vol% or more metal was failed as the particles experienced jamming in the narrow orifice of the extruder die as it approached the empirical random close packing (~64%) [43,44].

3.2. Homogeneity of metal dispersions

TGA was conducted on samples extracted at every two feet along the length of the continuously extruded 12 ft filaments, fabricated to examine the metal mass content and its spatial distribution. Multiple tests generated both the average and standard deviation of mass content and its values were converted to volumetric content (see Section 2.3 “Characterization” and Table S2 from the supplementary section for conversion details). Fig. 3A shows that the standard deviation of the metal’s spatial content gradually decreased with the increasing metal content irrespective of the mixing strategies due to the smaller mean free path for particle movement. Also, the filament’s average post-mix metal content (after extrusion) was closer to the pre-mix metal content (as mixed in the feedstock) in the case of solution mixing as compared to physical mixing. Note that, in Fig. 3A**,** a data point was taken for the physically-mixed sample of 56 vol% metal; although it did not pass our extrudability criterion because the filament broke during 12 feet continuous extrusion twice. However, extruded filaments were long and stable enough to measure their homogeneity. In Fig. 3B, the post-mix metal vol% trend (TGA outcome from the extruded filament section) along the filament length is shown. The volumetric metal content and its trend along the filament length has the potential to detect the early stages of material accumulation in the barrel. Thus, its spatial content was fitted with a line, and its slope is displayed in Fig. 3C. The rather chaotic and trendless values of the slopes suggest metal particle accumulation inside the extruder barrel to be unlikely. In Fig. 3D and E, different filament sections with comparable post-mix metal content are shown. Fig. 3D3 shows 56 vol% physically-mixed filament; it was not extrudable and windable according to our protocol, while Fig. 3E3 (solution-mixed sample) was still extrudable and windable without experiencing jamming or extrusion instability.

While the TGA analysis of the filament’s homogeneity on a global scale (i.e. along 12 ft long samples) revealed that both mixing strategies could extrude filaments continuously at a pre-mix content of 50 vol%, it raised the question of whether the suspension mixing inside the extruder’s barrel was sufficient to homogenize the physically-mixed feedstock or if the filaments had different degree of homogeneity. To answer this question, it was necessary to quantify the degree of homogeneity on a local scale between filaments prepared from precursors that were physically or solution-mixed from reconstructed 3D datasets obtained using X-ray computed microtomography (XCT). XCT scans were

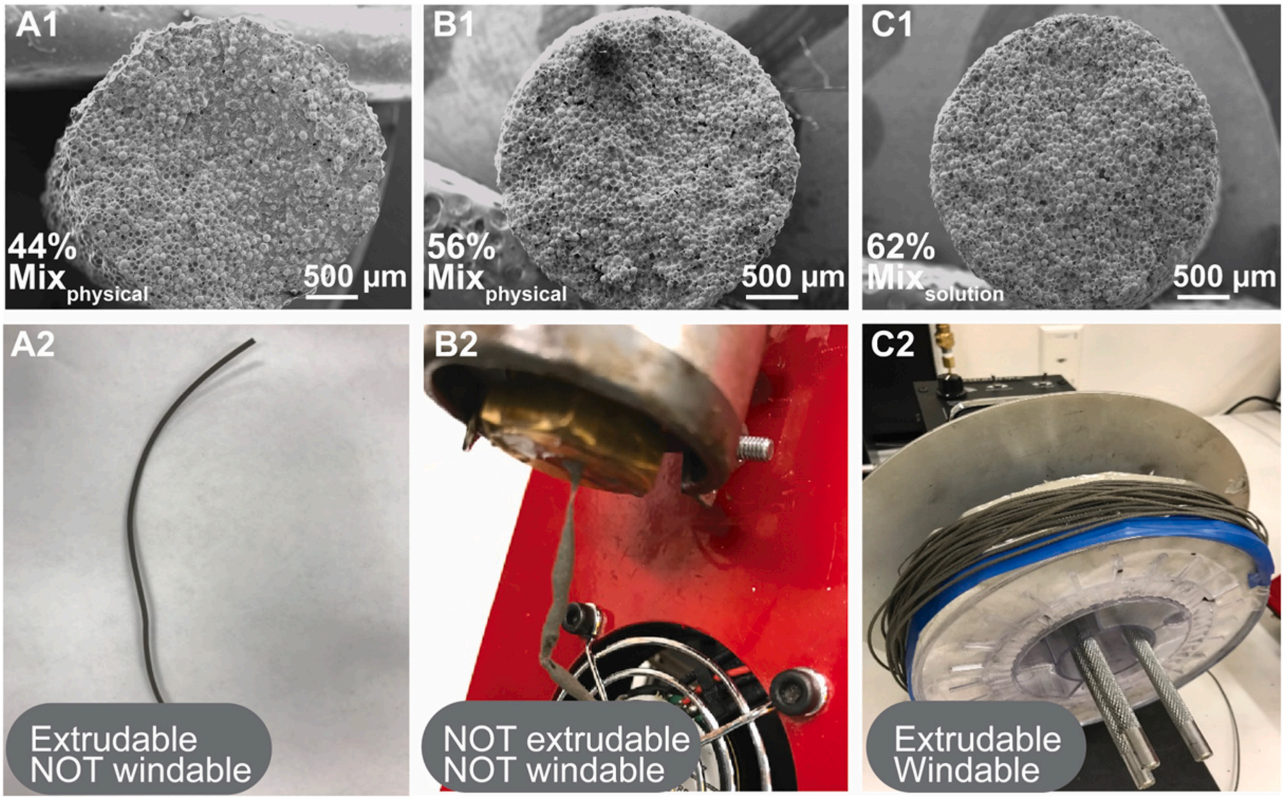

Fig. 2. Cross-sectional SEM images of extruded filaments with the pre-mix metal content of 44 vol% (A1), 56 vol% (B1) and 62 vol% (C1). Examples of filaments that illustrate the pass/fail extrudability and windability criteria (A2, B2, C2) with corresponding pre-mix metal content and feedstock mixing method as labeled in the first row (A1, B1, C1).

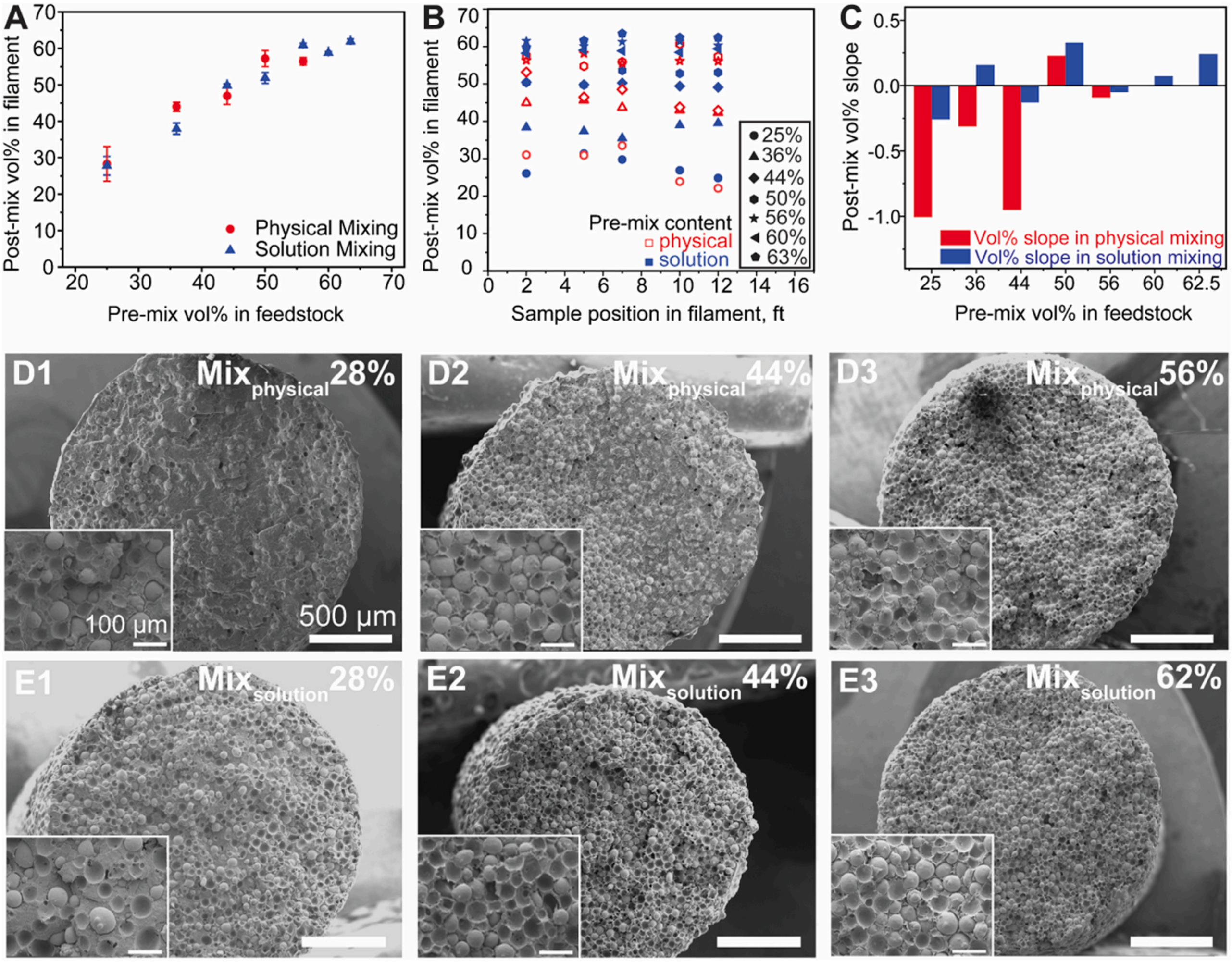

Fig. 3. Quantification of homogeneity of extruded filaments via TGA and cross-section SEM images: (A) actual (post-mix after extrusion) vs. designed (pre-mix) metal percentage, (B) metal vol% content in different positions along the 12 ft filament length, (C) slopes of slopes of post-mix metal vol% content extracted from linear fits along the filament length in (B), (D) cross-sectional images of physically-mixed metal filaments, and (E) solution-mixed metal filaments; higher magnification images are provided at insets. Pre-mix metal content and feedstock mixing method labeled in the top-right corner of every image in D and E.

performed on extruded filaments that were 25 vol% and 50 vol% in pre-mix metal content from both physically and solution-mixed feedstock. Cross-sectional XCT images from each sample set were shown in Fig. 4 (a) (b) (c) and (d), for each metal vol% (high pre-mix 50 vol% and low pre-mix 25 vol%) and mixing methods (physical and solution mixing) out of nearly 250 images taken by XCT.

Following the scan, the dataset was reconstructed using an in-house filtered back-projection algorithm. The gray values corresponding to the Ni-Cu powders were thresholded and segmented from the filament volume in the 3D datasets using Matlab. Finite body tessellation was performed using Euclidean distance maps to calculate the Coefficient of Variance (COV_d) of the mean nearest neighbor distance. Note that particles were considered to be neighbors if they share a cell wall that is equidistant between particles. The degree of clustering in the specimens (Fig. 4**e**) was measured through COV_d, which is defined as:

$$COVd = \frac{\sigma_d}{d}$$

where d is the average of the mean near neighbor distances between all particles and σ_d is the standard deviation of the mean near neighbor distances. The extent of clustering is proportional to the calculated COV_d value. A COV_d approaching 0 indicates a homogenous particle distribution and a random distribution of particles is characterized by a COV_d of ~0.36 [27,45]. Fig. 4(f) and (g) shows a comparison of the distribution of the mean neighbor distances and the number of neighbors for the 25 vol% physically-mixed and 25 vol% solution-mixed specimens. Both specimens show no significant differences in both distributions and COV_d values, indicating that the degree of clustering in both filaments (i.e. from solution and physically-mixed feedstocks) is similar. This implies that, although two different mixing strategies were employed, mixing inside the extruder by the action of the reciprocating screw is enough to homogenize the spatial distribution of the particles of the physically-mixed feedstock up to a pre-mix content of 50 vol%. This can be attributed to the large shearing stresses involved in extrusion as well as the relatively large volume fraction of particles that inherently causes the particles to be arranged in a homogeneous distribution. Thus, it can be concluded that solution mixing does prevent jamming and allows for the extrusion of uniform filaments with higher metal content (>54 vol%), but it does not produce more uniform filaments than physically-mixed feedstock in scenarios in which both feedstocks produce extrudable filaments.

3.3. *Effect on Rheology*

Spherical-shaped gas atomized metal powders were chosen due to their high flowability and to reduce the interlocking effects during extrusion. Both mixing methods produce filaments whose melt suspension viscosity scales with metal content, especially the zero-shear-rate

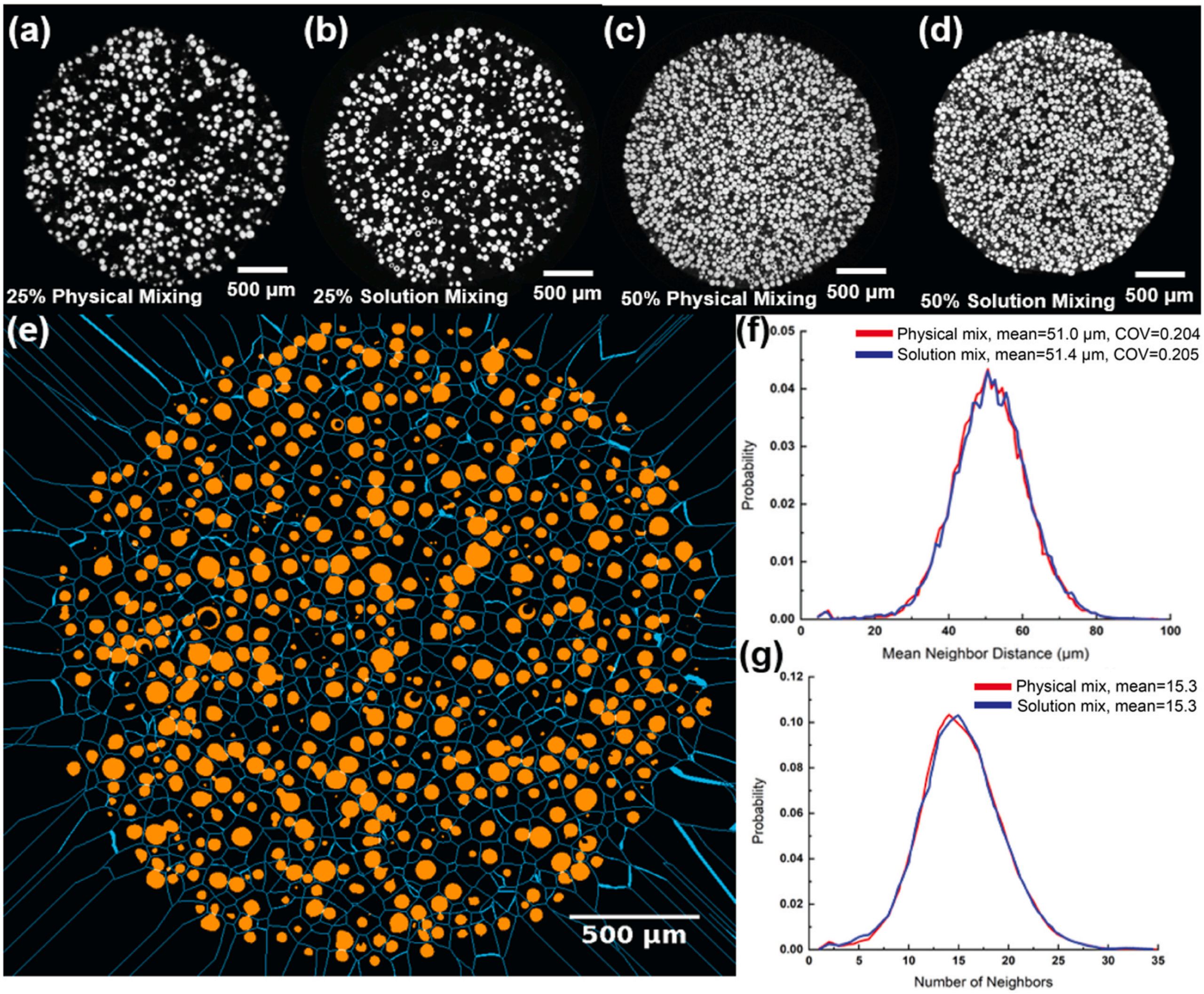

Fig. 4. Virtual cross-sections of extruded filaments obtained using XCT, (a) 25 vol% physical mixing, (b) 25 vol% solution mixing, (c) 50 vol% physical mixing, (d) 50 vol% solution mixing, (e) an example virtual cross-section of the 25% solution-mixed specimen showing the tessellation output with segmented particles (in orange) and cell walls between particles (in blue), (f) comparison of the distribution of mean neighbor distances and, (g) distribution of the number of nearest neighbors in extruded 25% physically-mixed and 25% solution-mixed filaments. (For interpretation of the references to color in this figure legend, the reader is referred to the web version of this article.)

viscosity (η_o) values (Fig. 5A and B). As compared to the melt suspension viscosity of the physically-mixed filaments, the solution-mixed filaments showed lower viscosity at the same shear rates and comparatively less steep plateau regions (below 55 vol% in Fig. 5A-B). For physical mixing above 58 vol% metals and at high shear rates (i.e. $> 10\ s^{-1}$), its viscosity drops more sharply in the shear-thinning region and its shear rate range shrinks, terminating at a shear rate of about $10\ s^{-1}$. While a lower viscosity in this case as compared to other cases with lower metal content would be considered an advantage for extrusion, the shear-thinning region terminates at a shear rate that is lower than the shear rates experienced during extrusion (i.e. $> 10\ s^{-1}$) through the die's small opening. Since the termination of the shear-thinning region is associated with the onset of slippage, it is argued that physically-mixed feedstock is more prone to slippage and unable to maintain the fluid's adherence to the wall and a velocity gradient along the radial direction of the die. This is the most plausible explanation for the poor extrudability test results associated with the physically-mixed feedstock (Table 2). With the increase of shear rate, polymer chains are dis-entangled, and they tend to align with the shear direction, and when all the polymer chains are aligned a second Newtonian plateau was attained [46]. These plateau regions were observed only in the lower metal concentration (up to 43 vol% of metals), and as the metal content continued to increase, these secondary plateau regions disappeared (Fig. 5A and B). This disappearance of the secondary plateau can be explained by the increasing restriction imposed by added metal particles, which creates the obstruction towards disentanglement and alignment as the polymers tend to coil around those metal particles. The highest metal concentration of the solution-mixed extrudable and windable filament was 62 vol %, which was found to be an outlier as its secondary plateau region reappears even though it had the steepest shear-thinning line and finally, its shear-thinning region extends into higher shear rates as compared to the physically-mixed filaments of the highest metal content (Fig. 5A). This means that the solution-mixed filament of 62 vol% can sustain much higher shear rates than any of the physically-mixed filaments without slippage. This could be translated to the exceptional ability of the 62 vol% solution-mixed sample to withstand a much higher shear rate than the physically-mixed sample before slippage occurs, which explains better extrudability characteristics observed in our previous extrusion test (Table 2 and Fig. 2C1 and C2). Conversely, if physically-mixed feedstock slips, it becomes more prone to jamming and, thus, this would explain its poor outcomes in the extrudability tests. It is worth noting that local (i.e., between metal particles) and global (i.

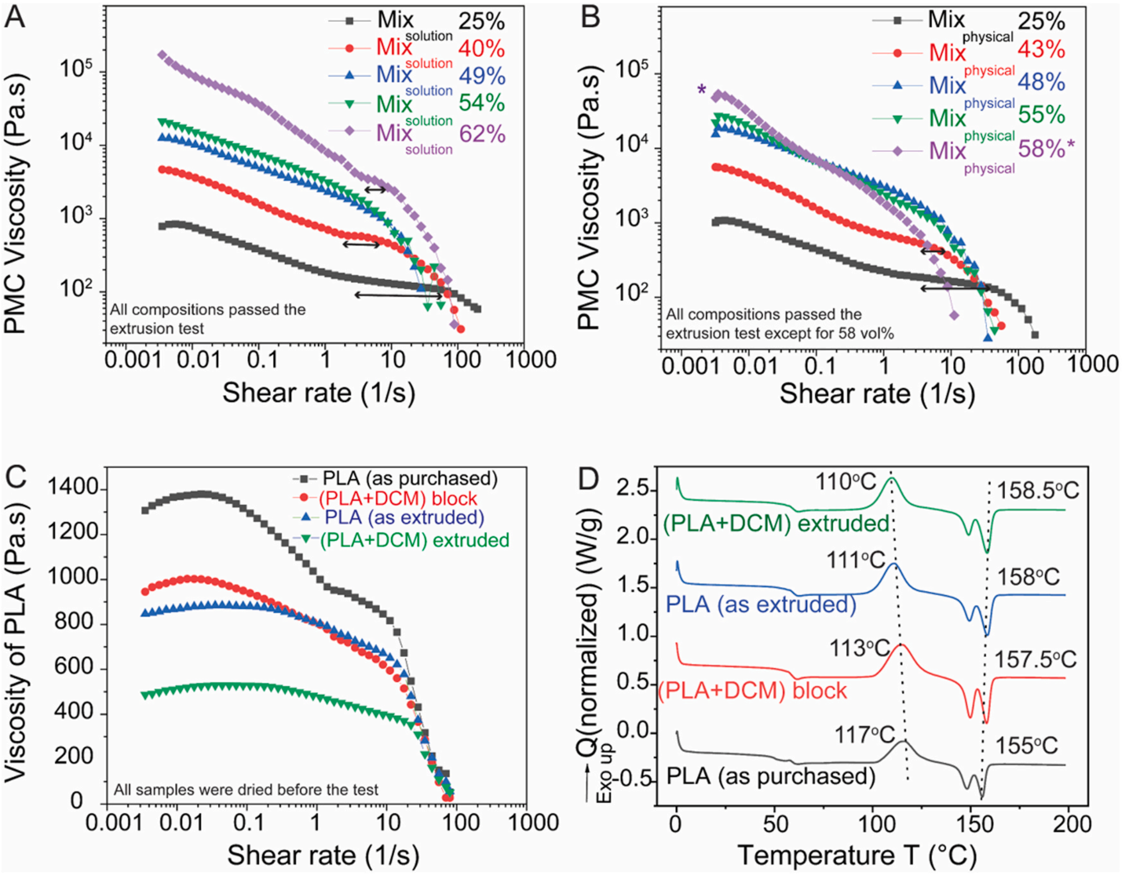

Fig. 5. Melt viscosity vs. shear rate at the different metal concentrations for filaments from (A) solution-mixing and (B) physical-mixing methods, (C) melt viscosity vs. shear rate of polymers at different processing states, and (D) DSC of pure PLA in different processing stages.

e., as measured by the rheometer) shear rates could also vary due to shear banding [47,48]. Metal concentrations of 63.5 vol% or greater led to extrusion failures due to jamming. At the microstructural level, it remains unproven why the PMC composite exhibits better adhesion to the walls of the rheometer or the extruder die. It is possible, albeit not proven, that the solution mixing step weakens secondary bonding between its polymer chains and allows them to disentangle more easily under shear and, thus, form a higher surface area contact to the extruder walls with better adhesion. This subject has been discussed in the literature [48].

To provide further insight into the effects of dissolution of PLA in solvent and extrusion of PLA during processing, the viscosity of pure PLA was measured: (i) as purchased PLA (ii) PLA after dissolving in DCM, (iii) pure PLA extrudate, and (iv) PLA extrudate after dissolving in DCM (Fig. 5C). Note that all samples were vacuum dried without the presence of solvent (Fig. 5C-D). Processed PLA dropped the zero-shear-rate viscosity from 1400 Pa-s for as-obtained to 1000 Pa-s and 900 Pa-s for dissolved PLA beads and extruded PLA filaments, respectively. Extrusion of dried PLA after dissolving in DCM further decreased this viscosity to 500 Pa-s for the zero-shear viscosity. This is attributed to the disentangled and aligned polymer chains provided by pre-dissolution and extrusion. For the case of thermoplastic (Fig. 5C), although dissolution in DCM helped to reduce the zero-shear viscosity of pure PLA by its intrinsic plasticizing effect, improvement of extrudability was not observed at higher shear rates (i.e. $> 30\ s^{-1}$) since all shear-thinning lines converged (Fig. 5C). Significant shear thinning (four orders of magnitude drop in dynamic viscosity) was evident in the case of suspensions (Fig. 5A/B) compared to the shear-thinning experienced by polymer (only an order of magnitude drop in dynamic viscosity, Fig. 5C). The flat plateau region in pure PLA (Fig. 5C) versus steep slopes in PLA/metal composites (Fig. 5A/B) implied the facilitation of shear-thinning from metal powders [49]. These two effects are associated with the notion that the local shear rates (i.e. in between two metal powders) might be much higher than the global shear rates (i.e. measured macroscopically) [50].

At the same time, DSC was collected to understand the influence of DCM and extrusion on the microstructure of PLA. DSC plots (Fig. 5D) showed the trend of cold crystallization (T_c), and melting point (T_m), as well as the degree of crystallinity (Xc) defined by where $Xc = (\Delta Hc+\Delta Hm) \times 100/\Delta Hm^0$; where ΔH_c and ΔH_m are the crystallization and melting enthalpy of PLA and ΔHm^0 is the enthalpy of fully crystallized PLA with infinite crystal thickness with a value of 93 J/g [51]. T_m and X_c increased with the introduction of DCM dissolution, drying, and extrusion (see Table S3 from the supplementary section for details). The double melting peak of PLA is signifying the two different ordering of crystallites [52]. X_c of DCM dissolved PLA increased substantially (by 23%) from the X_c computed for pure PLA beads, which could be an effect of solvent [53] and shear flow [53,54] during PLA dissolution in DCM or physical aging [53] during extended cooling of the DCM dissolved solid PLA chunk. Since all of our samples for the rheology tests were taken after extrusion and no distinguishable difference was seen in terms of X_c (only 0.5%, see Table S3 from the supplementary section) between the extruded sample of pure PLA and extruded sample of DCM dissolved PLA, logically, the influence of polymer crystallinity on the rheological scaling is considered negligible. Some researchers mentioned the degree of crystallinity can lead to higher viscosity [55,56] and crystallinity can reversely influence the plasticization [57]. However, the route of quantifying crystallinity in our PMC filament was not adopted and may be subject to future studies since the impact of crystal morphology on the rheological signature of suspension [58] is difficult to understand as they are decoupled with multiple variables [53] i.e. shear flow [59], geometric confinement [60], interparticle free spacing [61] and the presence or concentration of nanoparticles itself as a nucleate to crystalize [62].

3.4. Comparison of experimental zero-shear-rate viscosity with the analytical model

The experimentally measured η_o was compared with theoretical predictions based on the Krieger and Dougherty [39] analytical model Eq. (1).

$$\eta_0 = \eta_s\left(1-\frac{\varnothing}{\varnothing_m}\right)^{-[\eta]\cdot\,\varnothing_m} \tag{1}$$

where, $\varnothing_m$ indicates the maximum attainable packing fraction of spherical and rigid particles, $\varnothing$ is the volumetric packing fraction, η_s is the suspended liquid (in our case PLA polymer melt) viscosity and η_0 is the zero- shear-rate viscosity of the suspension (suspension with filled particles). $[\eta]$ is the intrinsic viscosity of suspension which is closely associated with the aspect ratio of the particles in terms of deviation from the ideal sphere [39]. As rigid and hard metal spheres were used in this case, the modified equation of Quemada [63] using $[\eta]\varnothing_m = 2$ is applicable here. For our case, variable metal content were used in $\varnothing$ values, random close packing (RCP) value of 0.64 was used as $\varnothing_m$, zero shear viscosity value of pure PLA extrudate (873 Pa.s) was used as η_s for physically-mixed samples and zero shear viscosity value of dried (PLA+DCM) extrudate (515 Pa.s) was used as η_s for solution-mixed samples to get the η_0 from the model and compared with the experimental η_0 to match the model. The experimentally measured η_o at different metal concentrations matches well with the Krieger and Dougherty analytical model, as seen in Fig. 6. Note that this is done without any fitting parameter and simply using parameters experimentally measured. Krieger and Dougherty's model of η_o predicts more accurately the experimental data of the solution-mixed feedstock than that of physically-mixed. The difference mainly stems from the distinction between the theoretically calculated zero shear viscosity of physical mixing cases and solution mixing cases, because in physical mixing suspending liquid viscosity η_s is higher than that of the solution mixing. Besides, solution-mixed feedstock could reach at higher metal content in filaments because unlike physical mixing it could be extruded without wall slippage, so it was possible to compare with the theoretical model at higher metal content. The close match with the theoretical model with a very high viscosity at higher metal concentration indicates that hydrodynamic forces dominate over the thermodynamic forces due to more particle-particle interactions and enhanced collision probabilities, which leads to the dramatic escalation of viscosity and the suspension starts to behave more like a solid at low shear rates as Ø approaches ~0.64, the dense random close packing (RCP) [44,64–66].

The physics of molten filled polymer suspension at higher filler concentration is extremely complex due to multi-body interactions [44, 67]. In the zero-shear rate limit, the maximum packing fraction is considered a 0.64, known as the random close packing limit. For the high shear rate limit, the maximum packing is typically considered 0.71, close to the maximum packing value of 0.74 for face-centered cubic (FCC) structure [44,65]. Smith and Zukoski [44] mentioned that in a very high packing limit near the RCP (0.64), zero-shear viscosity approaches infinity. Cassagnau [67] described this particular phenomenon of zero-shear viscosity diverging to infinity, which can be a result of forming a network structure from interparticle interaction. Our experimental outcome had a good agreement with that observation, as in our extrudability test we were unable to extrude 63.5 vol% or more metals, which signals the material behavior shift to elastic solid or in other words it exhibited infinite viscosity (see Fig. S4 from the supplementary section, for a piece of jammed materials that were taken out from the extruder barrel as a solid block). This extrusion failure phenomena can be explained in the light of jamming physics. As the packing fraction increases and approaches the critical limit, the type of interaction among the particles plays a stronger role over the interstitial liquid between particles. This sudden transition of flow behavior near the critical threshold packing is very complex to understand since depending on the flow history, the primary source of viscous dissipation can be generated from the friction of the adjacent particles if there is a contact network formed or it can be the outcome of hydrodynamic dissipation of interstitial liquid thin film [66]. Near the critical concentration, a subtle change in size and spatial distribution can suspend its ability to flow, which happens from the interlocking of the particles at the narrow orifice of the extruder die when there is strong particle-particle contact [68]. Majumdar et al. [69] explained this jamming transition phenomenon as an after-effect of small residual shear stresses developed from the interaction of particles and die wall. With the aid of numerical simulation, O'Hern et al. [70] concluded that the threshold packing fractions narrows its distribution curve and reaches a peak as it approaches random close packing and he explained that jamming stems from the extremely long stress relaxation time for highly loaded suspensions. van der Werff et al. [71] considered pairwise interactions of particles and concluded that the longest relaxation time becomes longer with increasing particle volume fraction making the mean relaxation time of suspension so high that it could be considered as elastic solid in finite observation time. Our SAOS test (described in the next section) also supports this evidence, as with the increase of metal concentration at a higher shear rate tanδ value diminishes which effectively

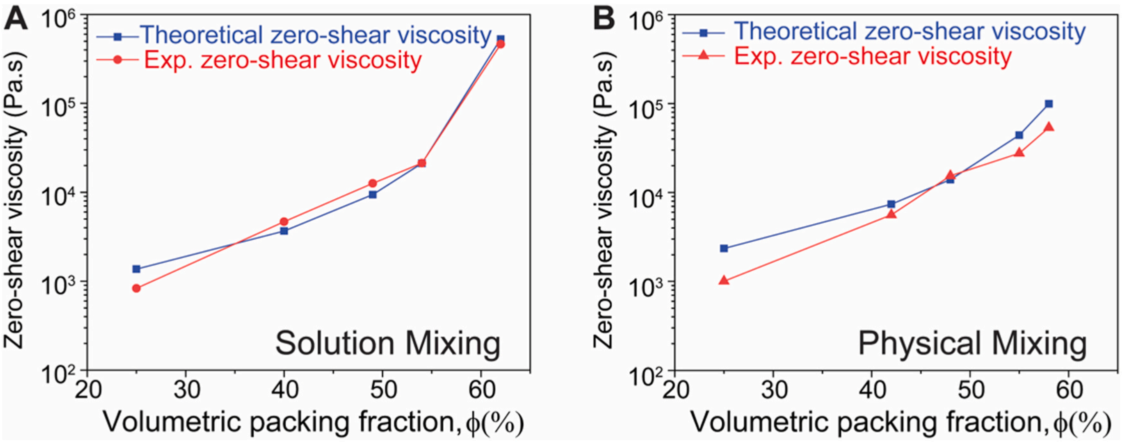

Fig. 6. Comparison of experimental zero-shear-rate viscosity with the analytical model of Krieger and Dougherty [39]: (A) solution-mixed samples, and (B) physically-mixed samples.

consolidates the fact that material behavior shifts from viscoelastic state to elastic solid-state making it impossible to flow.

3.5. Small Amplitude Oscillatory Shear test (SAOS)

To characterize the viscoelastic behavior and its transition of solution-mixed composites, SAOS test was employed as a function of metal content [40]. From the frequency sweep test, storage modulus (G′) and loss modulus (G″) were measured, allowing for the calculation of the damping parameter, (tanδ). Adding more metal particles increased both dynamic moduli over the entire range of frequency. The increase of frequency increased both the storage and loss modulus (Fig. 7A and B) because both the hydrodynamic force and inter-particle interaction were increased with higher shear rates [72]. Since metals were rigid and the global shear rate is concentrated in the narrow interstitial of the particles, even without the particle-particle interaction at increasing shear rate, elasticity of suspending fluid can influence the hydrodynamic effects with particle rotational movement, flow lines around the particles, and squeezing flow between interstitial particles [73]. At a very low inter-particle distance, a low-frequency plateau was observed in both dynamic moduli curves at the highest vol% of metals, which could be a signature of space-filling network structure [73] or pronounced connectivity [74]. The most distinct change of the tan δ values was the decrease of transition frequency and the depression of dampening parameters, as a function of metal vol% increase (Fig. 7C and D). With the increasing concentration of metals, depression of damping was observed which signifies that the suspension exhibits a more elastic behavior that arises from the stiffness of rigid fillers [75] and obstructs the polymer chain mobility requiring longer relaxation time. The earlier transition frequency observed for higher metal concentration signifies the earlier onset of elastic behavior at a lower frequency which has a good agreement with Lozano et al. [74] who claimed this comes from the effect of more pronounced connectivity among particles at higher concentration.

3.6. Debinding, sintering, and dimensional shrinkage analysis

Increasing the metal content of filaments to its absolute maximum is a rational strategy to minimize the part shrinkage during the post-processing (e.g., debinding and sintering) of metal-based material extrusion. This is one of the most critical drawbacks of metal FFF (Fused Filament Fabrication) that limits the dimensional integrity and tolerance of a printed part. To measure shrinkage, multiple 1 cm^3 cubes of varying metal concentrations were 3D printed (see the experimental **Section 2.2** and Table S4 from the supplementary section for more details), then debinded and sintered to quantify the linear shrinkage as a function of metal content. Note that no jamming was observed in the narrow orifice of the printer's head even when the 62 vol% metal filaments were used, which points out to the good printability of the solution-mixed filaments at higher metal content. To quantify the improvement of dimensional shrinkage, the highest extrudable and windable physically-mixed filament (43 vol%) and solution-mixed filament (62 vol%) were compared. The heat treatment cycle recipe contained a debinding step with a very slow heating rate of 0.2 °C/min to allow uniform heat penetration without destroying the cube structure. The debinding temperature was set slightly above (420 °C) the degradation temperature (around 400 °C, as measured by TGA) of PLA, to slowly boil the PLA without much agitation. Immediately after debinding, the sintering step was added with a heating rate of 5 °C/min ramping up to the sintering temperature (1061 °C), where the part was held for 5 h to allow coarsening of the particles and densification of the part structure. The sintering temperature was determined based on the available data [42] from the Ni–Cu alloy phase diagram, which is around 93% of the NiCu alloy melting point. The whole procedure was conducted in an ultra-high pure Argon atmosphere in a smelting graphite crucible surrounded by refractory

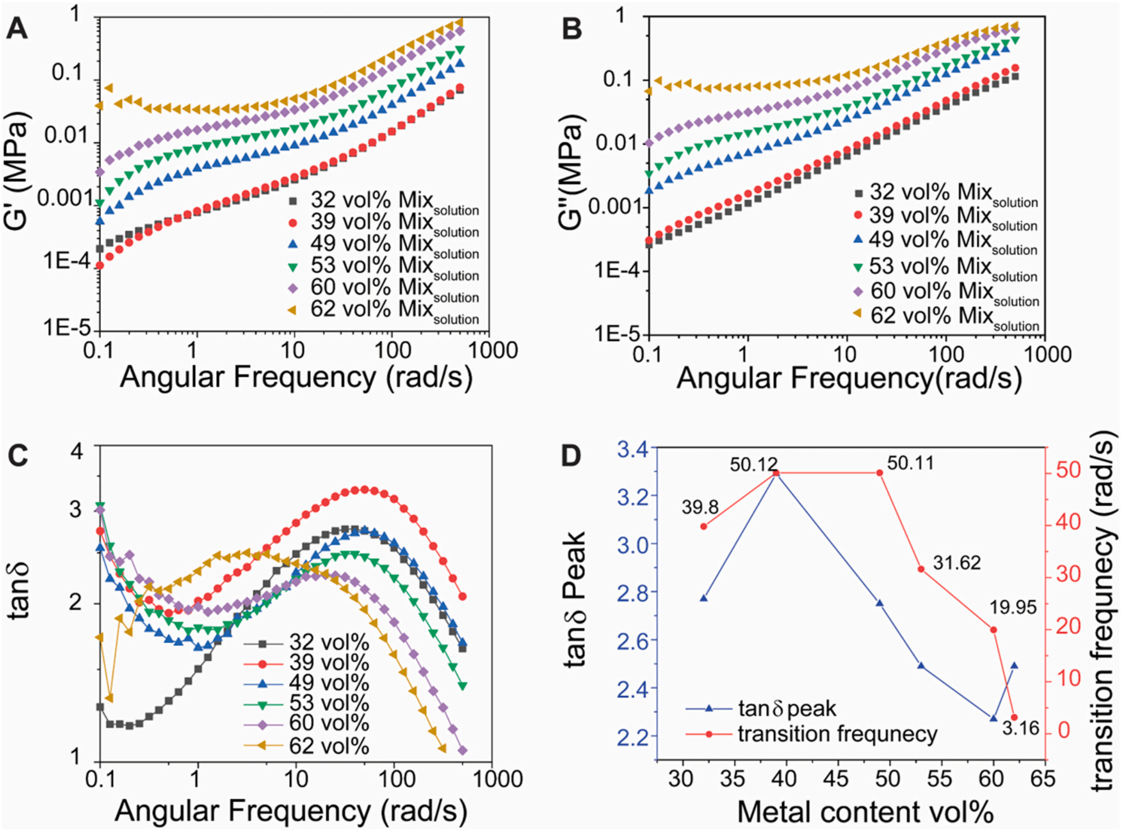

Fig. 7. SAOS test results of the melt suspension of solution-mixed filaments as a function increasing metal vol%:(A) storage modulus, (B) loss modulus, (C) damping factor and (D) tanδ and transition frequency.

ballast materials (a mixture of Al_2O_3 and graphite powders). The sintering ballast acted as a solid mold, allowing slow and uniform heat penetration to conform to the part's shape and maintain structural integrity. Since the samples were sintered in an inert atmosphere, only native oxides are expected to be present in the printed parts. As a result, the gray-color of the printed blocks matches that of the original NiCu alloy powders (see Supplementary Fig. S6). The linear shrinkage of the post-sintered part was significantly improved to 0.49% for the part printed with the 62 vol% solution-mixed filament, compared to the 2.02% shrinkage experienced by its counterpart printed with the 43 vol % physical mixed metal filament (Fig. 8). Note that, it is likely that more complex geometries different than a cuboid might have higher values. Thus, this accounts for a 76% reduction in the linear shrinkage in the sintered part. Although the part printed is still plagued by porosity inherent to material extrusion using metals, our experiment proved the potential of dimensional shrinkage improvement by homogeneously packing metals near the semi-empirical maximum packing fraction since dimensional shrinkage is inversely proportional to the initial metal content. The shrinkage values obtained here are close to those reported by commercially available filaments by Virtual Foundry [76] and are significantly lower than those reported in the literature [77–84], which is explained by the fact that this study employs an entire process scheme that most closely match that of commercial metal-based material extrusion process (i.e. feedstock material selection and mixing processes, debinding and sintering protocol, refractory powder support and atmosphere, and printing parameters).

The printed parts exhibit a density of 3.09 g/cc and 4.48 g/cc for the blocks printed from filaments with a metal content of 43 vol% (physically-mixed) and 62 vol% (solution-mixed), respectively. This result highlights the improved density that is achieved from increasing the volumetric metal content in the filaments at identical sintering conditions. While the sintered parts are still highly porous compared to the theoretical density of this alloy (9.84 g/cc), the added porosity is attributed to intra-track and inter-particle porosity common to the FFF process. Additional studies are needed to understand the improvements in densification [85,86] that can be achieved by increasing the sintering temperature and its trade-off with shrinkage. Finally, a cross-section of the metal 3D-printed block was made by polishing one of its facets and optical micrographs were taken along different regions of the cross-section to highlight the intra-track and intra-particle porosity (Fig. 8C). The morphology showed necking between particles and the porosity that is characteristic of metal FFF shown in multiple references [87,88]. This work has been limited to understanding the shrinkage effects of the densified green parts and more information on the strength and hardness of metal FFF parts can be found in the literature [89–91].

4. Conclusion

This study sheds light on the rheology scaling of extruded PMCs by tailoring the feedstock pre-mixing strategy. Attention was given to examine and compare two feedstock mixing strategies by analyzing their effects on the particle homogeneity, melt suspension viscosity, and filament extrudability. It was found that the solution mixing method is more effective than the physical mixing method in terms of the PMC's extrudability and windability as it has the rheological capability of avoiding wall slippage and jamming at higher metal content. However, local dispersion homogeneity of particles essentially remained the same for both higher (<55 vol%) and lower (25 vol%) metal content irrespective of the mixing strategy due to the effective shear mixing experienced inside the extruder. Even though the zero-shear viscosity of the solution-mixed 62 vol% filament was extremely high, it was still extrudable and windable, because it could sustain a higher shear rate without experiencing wall slippage, whereas physically-mixed filament could not sustain such a high shear rate and experienced unstable

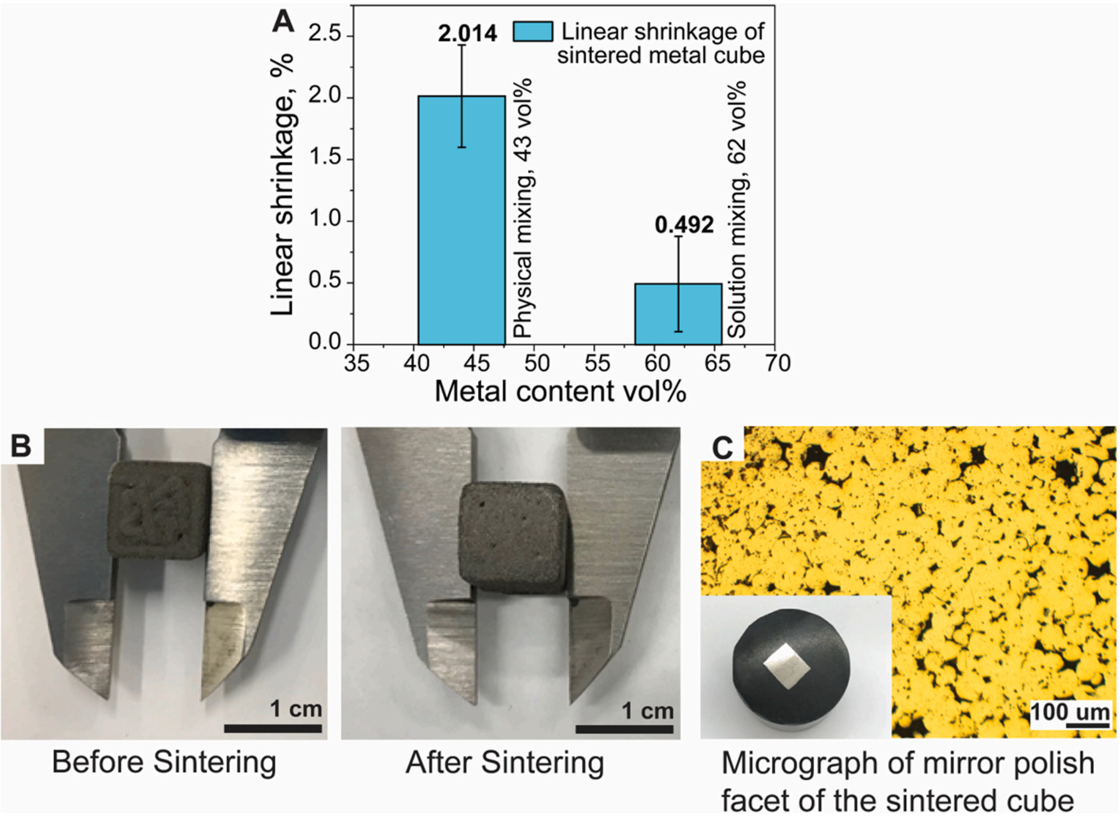

Before Sintering

After Sintering

Micrograph of mirror polish facet of the sintered cube

Fig. 8. Shrinkage assessment: (A) dimensional shrinkage minimization of sintered part by shifting to 62 vol% solution-mixed filament from 42 vol% physically-mixed filament, (B) printed part dimension measurements before and after sintering and (C) micrograph of mirror polish facet of the sintered cube with 62 vol % metal.

extrusion due to slippage at higher metal content leading to extrusion failure much before than 62 vol%. Our experimental results align well with the Krieger and Dougherty theoretical model developed for zero shear viscosity of filled polymer systems with rigid hard spheres. Also, the linear dimensional shrinkage of our printed parts was reduced by 76% after sintering for the highest filament content of 62 vol% (highest extrudable and windable filament from solution-mixed feedstock), compared to 43 vol% (highest extrudable and windable filament from physically-mixed feedstock). Above all, this study helps one to understand the synergistic impact of rheology scaling, particle homogeneity, and packing of metals in a polymer matrix as a limit to continuous extrudability, windability, and dimensional shrinkage of sintered part by metal additive manufacturing via material extrusion.

CRediT authorship contribution statement

Amm G. Hasib: Methodology, Validation, Formal analysis, Investigation, Writing - Original Draft, Visualization **Stanislau Niauzorau:** Methodology, Investigation **Weiheng Xu:** Methodology, Validation, Investigation **Sridhar Niverty:** Methodology, Software, Formal analysis, Writing - Review & Editing **Natalya Kublik:** Methodology, Investigation **Jason Williams:** Software, Data Curation **Nikhilesh Chawla:** Methodology, Conceptualization, Supervision, Resources, Writing – Review & Editing, Project Administration, Funding Acquisition; **Kenan Song:** Methodology, Conceptualization, Supervision, Resources, Writing – Original Draft, Writing – Review & Editing, Project Administration, Funding Acquisition; **Bruno Azeredo:** Methodology, Conceptualization, Supervision, Resources, Writing – Original Draft, Writing – Review & Editing, Project Administration, Funding Acquisition.

Declaration of Competing Interest

The authors declare that they have no known competing financial interests or personal relationships that could have appeared to influence the work reported in this paper.

Acknowledgments

We gratefully acknowledge the use of facilities within the Center for 4D Materials Science (4DMS), the LeRoy Eying Center for Solid State Science, and the John M Cowley High-Resolution Electron Microscopy Center at Arizona State University, the National Science Foundation under Grant No. CMMI-1932899 and the Arizona Board of Reagents' Innovation Fund Award No. AWD00034194.

Appendix A. Supporting information

Supplementary data associated with this article can be found in the online version at doi:10.1016/j.addma.2021.101967.

References

[1] D. Bak, Rapid prototyping or rapid production? 3D printing processes move industry towards the latter, Assem. Autom. 23 (2003) 340–345, https://doi.org/10.1108/01445150310501190.

[2] G. Loke, R. Yuan, M. Rein, T. Khudiyev, Y. Jain, J. Joannopoulos, Y. Fink, Structured multimaterial filaments for 3D printing of optoelectronics, Nat. Commun. 10 (2019) 4010, https://doi.org/10.1038/s41467-019-11986-0.

[3] N.K. Roy, D. Behera, O.G. Dibua, C.S. Foong, M.A. Cullinan, A novel microscale selective laser sintering (μ-SLS) process for the fabrication of microelectronic parts, Microsyst. Nanoeng. 5 (2019) 64, https://doi.org/10.1038/s41378-019-0116-8.

[4] J.H. Tan, W.L.E. Wong, K.W. Dalgarno, An overview of powder granulometry on feedstock and part performance in the selective laser melting process, Addit. Manuf. 18 (2017) 228–255, https://doi.org/10.1016/j.addma.2017.10.011.

[5] N.T. Aboulkhair, M. Simonelli, L. Parry, I. Ashcroft, C. Tuck, R. Hague, 3D printing of aluminium alloys: additive manufacturing of aluminium alloys using selective laser melting, Prog. Mater. Sci. 106 (2019), 100578, https://doi.org/10.1016/j.pmatsci.2019.100578.

[6] J.C. Heigel, P. Michaleris, E.W. Reutzel, Thermo-mechanical model development and validation of directed energy deposition additive manufacturing of Ti–6Al–4V, Addit. Manuf. 5 (2015) 9–19, https://doi.org/10.1016/j.addma.2014.10.003.

[7] H. Fayazfar, M. Salarian, A. Rogalsky, D. Sarker, P. Russo, V. Paserin, E. Toyserkani, A critical review of powder-based additive manufacturing of ferrous alloys: process parameters, microstructure and mechanical properties, Mater. Des. 144 (2018) 98–128, https://doi.org/10.1016/j.matdes.2018.02.018.

[8] W.J. Sames, F.A. List, S. Pannala, R.R. Dehoff, S.S. Babu, The metallurgy and processing science of metal, Int. Mater. Rev. 61 (2016) 315–360. 〈https://www.osti.gov/servlets/purl/1267051〉.

[9] J. Korpela, A. Kokkari, H. Korhonen, M. Malin, T. Narhi, J. Seppalea, Biodegradable and bioactive porous scaffold structures prepared using fused deposition modeling, J. Biomed. Mater. Res. Part B Appl. Biomater. 101 (2013) 610–619, https://doi.org/10.1002/jbm.b.32863.

[10] K.S. Boparai, R. Singh, H. Singh, Development of rapid tooling using fused deposition modeling: a review, Rapid Prototyp. J. 22 (2016) 281–299, https://doi.org/10.1108/RPJ-04-2014-0048.

[11] X. Wang, M. Jiang, Z. Zhou, J. Gou, D. Hui, 3D printing of polymer matrix composites: a review and prospective, Compos. Part B Eng. 110 (2017) 442–458, https://doi.org/10.1016/j.compositesb.2016.11.034.

[12] M.E. Mackay, The importance of rheological behavior in the additive manufacturing technique material extrusion, J. Rheol. (N.Y.) 62 (2018) 1549–1561, https://doi.org/10.1122/1.5037687.

[13] J.S. Park, T. Kim, W.S. Kim, Conductive cellulose composites with low percolation threshold for 3D printed electronics, Sci. Rep. 7 (2017) 1–10, https://doi.org/10.1038/s41598-017-03365-w.

[14] M.E. Sotomayor, A. Várez, B. Levenfeld, Influence of powder particle size distribution on rheological properties of 316L powder injection moulding feedstocks, Powder Technol. 200 (2010) 30–36, https://doi.org/10.1016/j.powtec.2010.02.003.

[15] R. Greenwood, P.F. Luckham, T. Gregory, Minimising the viscosity of concentrated dispersions by using bimodal particle size distributions, Colloids Surf. A Physicochem. Eng. Asp. 144 (1998) 139–147, https://doi.org/10.1016/S0927-7757(98)00409-9.

[16] R.S. Farr, R.D. Groot, Close packing density of polydisperse hard spheres, J. Chem. Phys. 131 (2009) 1–8, https://doi.org/10.1063/1.3276799.

[17] M. Kolonko, S. Raschdorf, D. Wäsch, A hierarchical approach to simulate the packing density of particle mixtures on a computer, Granul. Matter 12 (2010) 629–643, https://doi.org/10.1007/s10035-010-0216-5.

[18] D.F. Heaney, R. Zauner, C. Binet, K. Cowan, J. Piemme, Variability of powder characteristics and their effect on dimensional variability of powder injection moulded components, Powder Met. 47 (2004) 145–150, https://doi.org/10.1179/003258904225015491.

[19] Y. Yuan, L. Liu, Y. Zhuang, W. Jin, S. Li, Coupling effects of particle size and shape on improving the density of disordered polydisperse packings, Phys. Rev. E 98 (2018), 042903, https://doi.org/10.1103/PhysRevE.98.042903.

[20] B. Hausnerova, B.N. Mukund, D. Sanetrnik, Rheological properties of gas and water atomized 17-4PH stainless steel MIM feedstocks: effect of powder shape and size, Powder Technol. 312 (2017) 152–158, https://doi.org/10.1016/j.powtec.2017.02.023.

[21] L.M. Hamming, R. Qiao, P.B. Messersmith, L. Catherine Brinson, Effects of dispersion and interfacial modification on the macroscale properties of TiO2 polymer-matrix nanocomposites, Compos. Sci. Technol. 69 (2009) 1880–1886, https://doi.org/10.1016/j.compscitech.2009.04.005.

[22] A. Mannschatz, A. Müller, T. Moritz, Influence of powder morphology on properties of ceramic injection moulding feedstocks, J. Eur. Ceram. Soc. 31 (2011) 2551–2558, https://doi.org/10.1016/j.jeurceramsoc.2011.01.013.

[23] E. Fereiduni, A. Ghasemi, M. Elbestawi, Characterization of composite powder feedstock from powder bed fusion additive manufacturing perspective, Materials (Basel) (2019), https://doi.org/10.3390/ma12223673.

[24] R.P. Koseski, P. Suri, N.B. Earhardt, R.M. German, Y.S. Kwon, Microstructural evolution of injection molded gas- and water-atomized 316L stainless steel powder during sintering, Mater. Sci. Eng. A 390 (2005) 171–177, https://doi.org/10.1016/j.msea.2004.08.002.

[25] V. Khoshkava, M.R. Kamal, Effect of surface energy on dispersion and mechanical properties of polymer/nanocrystalline cellulose nanocomposites, Biomacromolecules 14 (2013) 3155–3163, https://doi.org/10.1021/bm400784j.

[26] G.D. Goh, Y.L. Yap, S. Agarwala, W.Y. Yeong, Recent progress in additive manufacturing of fiber reinforced polymer composite, Adv. Mater. Technol. 4 (2019) 1–22, https://doi.org/10.1002/admt.201800271.

[27] N. Yang, J. Boselli, I. Sinclair, Simulation and quantitative assessment of homogeneous and inhomogeneous particle distributions in particulate metal matrix composites, J. Microsc. 201 (2001) 189–200, https://doi.org/10.1046/j.1365-2818.2001.00766.x.

[28] G.A. Yakaboylu, E.M. Sabolsky, Determination of a homogeneity factor for composite materials by a microstructural image analysis method, J. Microsc. 266 (2017) 263–272, https://doi.org/10.1111/jmi.12536.

[29] R.R. Tiwari, U. Natarajan, Effect of organic modifiers and silicate type on filler dispersion, thermal, and mechanical properties of ABS-clay nanocomposites, J. Appl. Polym. Sci. 110 (2008) 2374–2383, https://doi.org/10.1002/app.28699.

[30] J. Xu, J.W. Bartels, D.A. Bohnsack, T.C. Tseng, M.E. Mackay, K.L. Wooley, Hierarchical inorganic-organic nanocomposites possessing amphiphilic and morphological complexities: influence of nanofiller dispersion on mechanical performance, Adv. Funct. Mater. 18 (2008) 2733–2744, https://doi.org/10.1002/adfm.200701490.

[31] T. Fujigaya, N. Nakashima, Methodology for homogeneous dispersion of single-walled carbon nanotubes by physical modification, Polym. J. 40 (2008) 577–589, https://doi.org/10.1295/polymj.PJ2008039.

[32] J. Masuda, J.M. Torkelson, Dispersion and major property enhancements in polymer/multiwall carbon nanotube nanocomposites via solid-state shear pulverization followed by melt mixing, Macromolecules 41 (2008) 5974–5977, https://doi.org/10.1021/ma801321j.

[33] J.M. Adames, Characterization of Polymeric Binders For Metal Injection Molding (MIM) Process, University of Akron, 2007, https://doi.org/10.1080/00102208008946937.

[34] X. Kong, Development and Characterization of Polymer-Metallic Powder Feedstocks for Micro-Injection Molding, Université de Franche-Comté, 2013.

[35] C.I. Chung. Extrusion of Polymers-Theory and Practice, 2nd ed., Hanser Publishers, Cincinnati, Munich, 2019 https://doi.org/10.3139/9781569907382.fm.

[36] D.G. Baird. Polymer Processing, 2nd ed., Willey, NJ, 2014 https://doi.org/10.1179/026708303225004738.

[37] J. Gonzalez-Gutierrez, I. Duretek, C. Holzer, F. Arbeiter, C. Kukla, Filler content and properties of highly filled filaments for fused filament fabrication of magnets, Annu. Tech. Conf. - ANTEC, Conf. Proc. 2017-May (2017) 55–58.

[38] S.K. Jain, Y. Tadesse, Fabrication of polylactide/carbon nanopowder filament using melt extrusion and filament characterization for 3D printing, Int. J. Nanosci. 18 (2019) 1–4, https://doi.org/10.1142/S0219581X18500266.

[39] I.M. Krieger, T.J. Dougherty, A mechanism for non-newtonian flow in suspensions of rigid spheres, Trans. Soc. Rheol. 3 (1959) 137–152, https://doi.org/10.1122/1.548848.

[40] K.P. Menard. Dynamic Mechanical Analysis: A Practical Introduction, 2nd ed., CRC Press, Boca Raton, London, New York, Washington D.C, 2008.

[41] E. Baran, H. Erbil, Surface modification of 3D printed PLA objects by fused deposition modeling: a review, Colloids Interfaces 3 (2019) 43, https://doi.org/10.3390/colloids3020043.

[42] Vacarro W., Copper-Nickel Example, MSE2094_Notebook. (1996). ⟨http://sv.rkriz.net/classes/MSE2094_NoteBook/96ClassProj/OLD/examples/cu-ni.html⟩ (accessed August 17, 2020).

[43] W. Pabst, Fundamental considerations on suspension rheology, Ceram. Silikaty 48 (2004) 6–13.

[44] W.E. Smith, C.F. Zukoski, Flow properties of hard structured particle suspensions, J. Rheol. (N.Y.) 48 (2004) 1375–1388, https://doi.org/10.1122/1.1807846.

[45] A. Ayyar, G.A. Crawford, J.J. Williams, N. Chawla, Numerical simulation of the effect of particle spatial distribution and strength on tensile behavior of particle reinforced composites, Comput. Mater. Sci. 44 (2008) 496–506, https://doi.org/10.1016/j.commatsci.2008.04.009.

[46] T.A. Osswald, N. Rudolph, Polymer Rheology, Fundamentals and Applications, 1st Ed., First, Hanser Publishers, Munich, 2015 https://doi.org/10.1002/app.1961.070051418.

[47] G. Ovarlez, S. Rodts, X. Chateau, P. Coussot, Phenomenology and physical origin of shear localization and shear banding in complex fluids, Rheol. Acta 48 (2009) 831–844, https://doi.org/10.1007/s00397-008-0344-6.

[48] M. Cloitre, R.T. Bonnecaze, A review on wall slip in high solid dispersions, Rheol. Acta 56 (2017) 283–305, https://doi.org/10.1007/s00397-017-1002-7.

[49] B.G. Compton, J.A. Lewis, 3D-printing of lightweight cellular composites, Adv. Mater. 26 (2014) 5930–5935, https://doi.org/10.1002/adma.201401804.

[50] H.M. Laun, Orientation effects and rheology of short glass fiber-reinforced thermoplastics, Colloid Polym. Sci. 262 (1984) 257–269, https://doi.org/10.1007/BF01410464.

[51] S. Sato, D. Gondo, T. Wada, S. Kanehashi, K. Nagai, Effects of various liquid organic solvents on solvent-induced crystallization of amorphous poly(lactic acid) film, J. Appl. Polym. Sci. 129 (2013) 1607–1617, https://doi.org/10.1002/app.38833.

[52] N.L. Batista, P. Olivier, M.C. Rezende, E.C. Botelho, R. Talim, Correlation between degree of crystallinity, morphology and mechanical properties of PPS / carbon fiber laminates, 19 (2016) 195–201.

[53] S. Andjelic, R.C. Scogna, Polymer crystallization rate challenges: the art of chemistry and processing, J. Appl. Polym. Sci. 132 (2015) 1–15, https://doi.org/10.1002/app.42066.

[54] A.M. Rhoades, A.M. Gohn, J. Seo, R. Androsch, R.H. Colby, Sensitivity of polymer crystallization to shear at low and high supercooling of the melt, Macromolecules 51 (2018) 2785–2795, https://doi.org/10.1021/acs.macromol.8b00195.

[55] W.-F. Su, Principles of Polymer Design and Synthesis, in: Struct. Morphol. Flow Polym., vol 82., Berlin,Heidelberg, 2013: pp. 27–59. https://doi.org/10.1007/978–3-642–38730-2_3.

[56] G. Lamberti, G.W.M. Peters, G. Titomanlio, Crystallinity and linear rheological properties of polymers, Int. Polym. Process. 22 (2007) 303–310, https://doi.org/10.3139/217.2006.

[57] E.H. IMMERGUT, H.F. MARK, Principles of Plasticization, (1965) 1–26. https://doi.org/10.1021/ba-1965–0048.ch001.

[58] P. He, W. Yu, C. Zhou, Agglomeration of crystals during crystallization of semicrystalline polymers: a suspension-based rheological study, Macromolecules 52 (2019) 1042–1054, https://doi.org/10.1021/acs.macromol.8b02452.

[59] R.J.A. Steenbakkers, G.W.M. Peters, Suspension-based rheological modeling of crystallizing polymer melts, Rheol. Acta 47 (2008) 643–665, https://doi.org/10.1007/s00397-008-0273-4.

[60] A.M. Jimenez, A.A. Krauskopf, R.A. Pérez-Camargo, D. Zhao, J. Pribyl, J. Jestin, B. C. Benicewicz, A.J. Müller, S.K. Kumar, Effects of hairy nanoparticles on polymer crystallization kinetics, Macromolecules 52 (2019) 9186–9198, https://doi.org/10.1021/acs.macromol.9b01380.

[61] A. Jabbarzadeh, The origins of enhanced and retarded crystallization in nanocomposite polymers, Nanomaterials 9 (2019) 1–13, https://doi.org/10.3390/nano9101472.

[62] K. Hwa Yoon, S. Park, Y. Cheol Kim, Study of the rheological properties and crystallization behavior of branched PP/silicate composites, Polym. J. 44 (2012) 1098–1104, https://doi.org/10.1038/pj.2012.68.

[63] D. Quemada, Rheology of concentrated disperse systems II. A model for non-newtonian shear viscosity in steady flows, Rheol. Acta 17 (1978) 632–642, https://doi.org/10.1007/BF01522036.

[64] D.B. Genovese, Shear rheology of hard-sphere, dispersed, and aggregated suspensions, and filler-matrix composites, Adv. Colloid Interface Sci. 171–172 (2012) 1–16, https://doi.org/10.1016/j.cis.2011.12.005.

[65] J. Bicerano, J.F. Douglas, D.A. Brune, Model for the viscosity of particle dispersions, J. Macromol. Sci. Rev. Macromol. Chem. Phys. 39C (1999) 561–642, https://doi.org/10.1081/mc-100101428.

[66] P. Coussot, Introduction to the rheology of complex fluids, in: Underst. Rheol. Concr., Woodhead Publishing, 2012, pp. 3–22, https://doi.org/10.1533/9780857095282.1.3.

[67] P. Cassagnau, Linear viscoelasticity and dynamics of suspensions and molten polymers filled with nanoparticles of different aspect ratios, Polym. (Guildf.) 54 (2013) 4762–4775, https://doi.org/10.1016/j.polymer.2013.06.012.

[68] D.M. Kalyon, S. Aktaş, Factors affecting the rheology and processability of highly filled suspensions, Annu. Rev. Chem. Biomol. Eng. 5 (2014) 229–254, https://doi.org/10.1146/annurev-chembioeng-060713-040211.

[69] T.S. Majmudar, M. Sperl, S. Luding, R.P. Behringer, Jamming transition in granular systems, Phys. Rev. Lett. 98 (2007), 058001, https://doi.org/10.1103/PhysRevLett.98.058001.

[70] C.S. O'Hern, S.A. Langer, A.J. Liu, S.R. Nagel, Random packings of frictionless particles, Phys. Rev. Lett. 88 (2002) 4, https://doi.org/10.1103/PhysRevLett.88.075507.

[71] J.C. Van Der Werff, C.G. De Kruif, C. Blom, J. Mellema, Linear viscoelastic behavior of dense hard-sphere dispersions, Phys. Rev. A 39 (1989) 795–807, https://doi.org/10.1103/PhysRevA.39.795.

[72] A.I. Barzic, S. Loan, Viscoelastic Behavior of Liquid-Crystal Polymer in Composite Systems (in:), Intech, 2016, pp. 2–19, https://doi.org/10.5772/64074 (in:).

[73] J.F. Le Meins, P. Moldenaers, J. Mewis, Suspensions in polymer melts. 1. Effect of particle size on the shear flow behavior, Ind. Eng. Chem. Res. 41 (2002) 6297–6304, https://doi.org/10.1021/ie020117r.

[74] K. Lozano, S. Yang, Q. Zeng, Rheological analysis of vapor-grown carbon nanofiber-reinforced polyethylene composites, J. Appl. Polym. Sci. 93 (2004) 155–162, https://doi.org/10.1002/app.20443.

[75] M. Kumar, N. Shanmuga Priya, S. Kanagaraj, G. Pugazhenthi, Melt rheological behavior of PMMA nanocomposites reinforced with modified nanoclay, Nanocomposites 2 (2016) 109–116, https://doi.org/10.1080/20550324.2016.1221876.

[76] M. Petch, 3D printing metal on a desktop FDM printer, exclusive interview with The Virtual Foundry founder - 3D Printing Industry, 3D Print. Indus. (2017). ⟨https://3dprintingindustry.com/news/3d-printing-metal-desktop-fdm-printer-exclusive-interview-virtual-foundry-founder-103672/⟩. accessed August 17, 2020.

[77] H. Gong, D. Snelling, K. Kardel, A. Carrano, Comparison of stainless steel 316L parts made by FDM- and SLM-based additive manufacturing processes, JOM 71 (2019) 880–885, https://doi.org/10.1007/s11837-018-3207-3.

[78] Mukesh K. Agarwala, Vikram R. Jamalabad, Noshir A. Langrana, Ahmad Safari, Philip J. Whalen, Stephen C. Danforth, Structural quality of parts processed by fused deposition, Rapid Prototyp. J. 2 (1996) 4–19.

[79] C. Burkhardt, P. Freigassner, O. Weber, P. Imgrund, S. Hampel, Fused filament fabrication (FFF) of 316L green parts for the MIM process, World PM 2016 Congr. Exhib. 1 (2016).

[80] T. Ozel, P.J. Bartolo, E. Ceretti, J. de C. Gay, C.A. Rodriguez, J.V.L. Da Silva. Biomedical Devices, 1st ed., Wiley, 2016 https://doi.org/10.1002/9781119267034.

[81] M. Annoni, H. Giberti, M. Strano, Feasibility study of an extrusion-based direct metal additive manufacturing technique, Procedia Manuf. 5 (2016) 916–927, https://doi.org/10.1016/j.promfg.2016.08.079.

[82] B. Liu, Y. Wang, Z. Lin, T. Zhang, Creating metal parts by fused deposition modeling and sintering, Mater. Lett. 263 (2020), 127252, https://doi.org/10.1016/j.matlet.2019.127252.

[83] S. Onagoruwa, S. Bose, A. Bandyopadhyay, Fused deposition of ceramics (FDC) and composites, Proc. Solid Free. Fabr. Symp. (2001) 224–231. ⟨http://edge.rit.edu/edge/P10551/public/SFF/SFF2001Proceedings/2001SFF Papers/26-Onagoruwa.pdf⟩.

[84] S. Terry, I. Fidan, K. Tantawi, Dimensional Analysis of Metal Powder Infused Filament - Low Cost Metal 3D Printing, Solid Free. Fabr. Symp. Proc. (2019).

[85] H. Wu, W. Liu, L. Lin, Y. Li, Z. Tian, G. Nie, D. An, H. Li, C. Wang, Z. Xie, S. Wu, Sintering kinetics involving densification and grain growth of 3D printed Ce–ZrO2/Al2O3, Mater. Chem. Phys. 239 (2020) 1–6, https://doi.org/10.1016/j.matchemphys.2019.122069.

[86] Z. Xu, M.A. Hodgson, K. Chang, G. Chen, X. Yuan, P. Cao, Effect of sintering time on the densification, microstructure, weight loss and tensile properties of a powder metallurgical Fe–Mn–Si alloy, Metals (Basel) (2017), https://doi.org/10.3390/met7030081.

[87] Y. Zhang, S. Bai, M. Riede, E. Garratt, A. Roch, A comprehensive study on fused filament fabrication of Ti–6Al–4V structures, Addit. Manuf. 34 (2020), 101256, https://doi.org/10.1016/j.addma.2020.101256.

[88] P.K. Gurrala, S.P. Regalla, Part strength evolution with bonding between filaments in fused deposition modelling, Virtual Phys. Prototyp. 9 (2014) 141–149, https://doi.org/10.1080/17452759.2014.913400.

[89] S. Fafenrot, N. Grimmelsmann, M. Wortmann, A. Ehrmann, Three-dimensional (3D) printing of polymer-metal hybrid materials by fused deposition modeling, Materials (Basel) (2017), https://doi.org/10.3390/ma10101199.

[90] Z. Liu, Q. Lei, S. Xing, Mechanical characteristics of wood, ceramic, metal and carbon fiber-based PLA composites fabricated by FDM, J. Mater. Res. Technol. 8 (2019) 3743–3753, https://doi.org/10.1016/j.jmrt.2019.06.034.

[91] D. Godec, S. Cano, C. Holzer, J. Gonzalez-Gutierrez, Optimization of the 3D printing parameters for tensile properties of specimens produced by fused filament fabrication of 17-4PH stainless steel, Materials (Basel) (2020), https://doi.org/10.3390/ma13030774.